3-27-1998

Full-wave Modeling of Small-scale Gravity Waves using Airborne Lidar and Observations of the Hawaiian Airglow (ALOHA-93) O(¹S) Images and Coincident Na Wind/temperature Lidar Measurements

Michael P. Hickey Ph.D.
Embry-Riddle Aeronautical University, hicke0b5@erau.edu

Michael J. Taylor
Utah State University

Chester S. Gardner
University of Illinois at Urbana-Champaign

Christian R. Gibbons
University of Alabama - Huntsville

Scholarly Commons Citation

Hickey, M. P., M. J. Taylor, C. S. Gardner, and C. R. Gibbons (1998), Full-wave modeling of small-scale gravity waves using Airborne Lidar and Observations of the Hawaiian Airglow (ALOHA-93) O(1 S) images and coincident Na wind/temperature lidar measurements, J. Geophys. Res., 103(D6), 6439–6453, doi: https://doi.org/10.1029/97JD03373

JOURNAL OF GEOPHYSICAL RESEARCH, VOL. 103, NO. D6, PAGES 6439-6453, MARCH 27, 1998

Full-wave modeling of small-scale gravity waves using Airborne Lidar and Observations of the Hawaiian Airglow (ALOHA-93) O(^1S) images and coincident Na wind/temperature lidar measurements

Michael P. Hickey[1], Michael. J. Taylor[2], Chester S. Gardner[3], and Christian R. Gibbons[1]

Abstract. Measurements were made of mesospheric gravity waves in the OI (5577 Å) nightglow observed from Maui, Hawaii, during the Airborne Lidar and Observations of Hawaiian Airglow (ALOHA-93) campaign. Clear, monochromatic gravity waves were observed on several nights. By using a full-wave model that realistically includes the major physical processes in this region, we have simulated the propagation of four waves through the mesopause region and calculated the O(^1S) nightglow response to the waves. Mean winds derived from Na wind/temperature lidar observations were employed in the computations. Wave amplitudes were calculated based on the requirement that the observed and simulated relative airglow fluctuation amplitudes be equal. Although the extrinsic (i.e., observed) characteristics of all four waves studied were quite similar (horizontal wavelengths ~20 to 30 km; periods ~9 min; horizontal phase speeds ~35 to 50 m s^{-1}), the propagation characteristics of the waves are all quite different due to the different background mean winds through which the waves propagate. Three of the waves encounter critical levels in the mesopause region. For two of these waves the upward propagation beyond the 97 km level is severely impeded by their critical levels because the local value of the Richardson number exceeds unity there. The third wave is not severely attenuated at its critical level because the Richardson number there is about 0.25. The fourth wave does not encounter a critical level although it is strongly Doppler shifted to low frequencies over a limited height range by the mean winds. It appears to be able to propagate at least to the 110 km level essentially unimpeded. This study demonstrates that an accurate description of the mean winds is an essential requirement for a complete interpretation of observed wave-driven airglow fluctuations. The study also emphasizes that although the measured extrinsic properties of waves may be similar, their propagation to higher altitudes depends very sensitively on the mean winds through which the waves propagate.

1. Introduction

Recently, *Hickey et al.* [1997] simulated the response of the O(^1S) nightglow to mesospheric gravity waves that were measured over Arecibo, Puerto Rico, during the 10-day January 1993 campaign. The wave parameters required for the modeling were derived from the two-dimensional (2-D), all-sky images of *Taylor and Garcia* [1995]. A full-wave model was employed for the study, and several sets of mean winds were investigated for use in the model in order to determine the sensitivity of the derived wave amplitudes and their height variations to the assumed winds. The winds employed by *Hickey et al.* [1997] were derived from incoherent scatter radar (ISR) measurements, wind imaging interferometer (WINDII) measurements, and the climatological mean winds from the Cospar International Reference Atmosphere (CIRA) model [1990]. By normalizing the simulated O(^1S) nightglow intensity fluctuation amplitude to that observed by *Taylor and Garcia* [1995], *Hickey et al.* [1997] were able to derive altitude profiles of gravity wave amplitude. It was found that the derived wave amplitudes depended strongly on the particular mean wind profile employed in the simulation.

A significant aspect of the study of *Hickey et al.* [1997] was that the only available measured winds were not coincident in either time or location with the nightglow imager measurements. It was concluded that the mean wind was probably the single most important adjustable model parameter required for an accurate simulation of the observed nightglow variations and that without it the wave amplitudes derived from such a simulation are subject to considerable uncertainty. *Hickey et al.* [1997] also concluded that accurate mean wind information will be required over a significant altitude range in order to accurately describe and characterize the coupling by gravity waves between atmospheric regions. The transport of wave energy between different atmospheric regions is sensitive to the intervening atmospheric winds due to its dependence on the square of the wave amplitude.

[1]Center for Space Plasma, Aeronomy and Astrophysics Research, University of Alabama in Huntsville.
[2]Space Dynamics Laboratory, Utah State University, Logan.
[3]Department of Electrical and Computer Engineering, University of Illinois, Urbana.

Paper number 97JD03373.
0148-0227/98/97JD-03373$09.00

In this study we model waves observed over Maui, Hawaii, during the Airborne Lidar and Observations of Hawaiin Airglow (ALOHA-93) campaign. The small-scale gravity waves were measured in the O(^1S) nightglow emission with an all-sky 2-D imaging system [e.g., *Taylor et al.*, 1997], providing the wave parameters required for our full-wave/nightglow interaction model calculations. The mean winds in the vicinity of the O(^1S) nightglow emission layer (~97 km altitude) were measured with a Na wind/temperature lidar described by *Gardner et al.* [1995] and *Tao and Gardner* [1995]. Our simulations are performed using a realistic full-wave model describing wave propagation in an inhomogeneous atmosphere. It includes dissipation due to both eddy and molecular diffusion processes and the effects of mean background winds [*Hickey et al.*, 1994, 1995, 1997]. The full-wave model is coupled to a wave/nightglow interaction model, allowing us to calculate the response of a particular nightglow emission to a gravity wave. As in the work of *Hickey et al.* [1997], the main objective of the present study is to determine wave amplitude indirectly from the nightglow imager measurements. Unlike the previous study, however, the mean winds employed in the present simulations are coincident in both time and space with the airglow observations, and so are essentially those experienced by the measured waves. This study allows us to calculate the effects of the mean background winds on the observed gravity waves. Winds are known to have a significant effect on wave propagation, causing wave propagation to be anisotropic [e.g., *Cowling et al.*, 1971; *Taylor et al.*, 1993]. We will show that although the extrinsic (i.e., observed) properties of the simulated waves are all quite similar, the propagation characteristics of the waves are all dissimilar due to the effects of the different mean winds through which the waves propagate. In particular, we will demonstrate that the wave coupling between the mesopause region and the lower thermosphere depends very sensitively on the mean winds.

The layout of this paper is as follows. In section 2 the pertinent observations from the ALOHA-93 campaign are described. The full-wave model and the O(^1S) nightglow fluctuation model are briefly described in section 3, with more details given in an appendix. This is followed by the results section, which comprises a detailed numerical analysis for each of the observed waves. Following this, we conclude by discussing the limitations of the approach and suggest some possible improvements for future wave measurement campaigns.

2. ALOHA-93 Campaign Observations

The ALOHA-93 campaign provided a unique opportunity to study in detail wave motions in the mesosphere with a variety of instruments. The waves were observed in the O(^1S) nightglow emission using an all-sky imager [*Taylor et al.*, 1997]. The modeling of these waves also requires knowledge of the winds at the altitude of the observations. The winds were measured with a Na lidar which is described by *Gardner et al.* [1995] and *Tao and Gardner* [1995]. The observations were all obtained at Maui, Hawaii (20.8°N, 156.2°W), on the nights of October 7, 20, and 21, 1993.

2.1. All-Sky Image Observations

2.1.1. Instrumentation and operational details. During the ALOHA-93 campaign simultaneous Na wind/temperature lidar and airglow image measurements were made from the summit of Haleakala Crater, Maui, Hawaii (20.8°N, 156.2°W, 3050 m). The imager was located at the Department of Energy (DOE) Facility ~200 m from the lidar which was installed at the Air Force Maui Optic Site (AMOS). Coordinated observations were made from October 6-20, and a variety of waves were observed. For this study we have selected four wave events for detailed analysis that were recorded at the beginning (October 7) and toward the end of the campaign (October 20 and 21) under considerably different wind conditions. Wind and temperature measurements are described in the next section.

Coincident all-sky (180°) airglow image measurements of gravity wave structure were made over a similar altitude range by sampling four nightglow emissions that exhibit peak intensities at closely spaced, but different heights: the near-infrared (715-930 nm) OH bands at ~87 km, the O_2 (0,1) atmospheric band (~865 nm) at ~94 km, the OI (557.7 nm) line at ~96 km, and the Na (589.2 nm) lines at ~90 km. The camera utilized a high-performance solid state (CCD) array of 1024 x 1024 pixels back-thinned to provide a high quantum efficiency of ~80% at visible wavelengths and ~50% at NIR wavelengths. The digital data were binned down to 512 x 512 pixels providing a zenith horizontal spatial resolution of ~0.6 km over the 80-100 height range. Sequential measurements of each emission were made using a computer-controlled filter wheel coupled to a telecentric lens arrangement permitting wide field measurements using narrow band filters (typically 1.5 nm). Further information describing the imaging system is given by *Taylor et al.* [1997]. For the ALOHA-93 campaign integration times of 20 s for the bright OH bands, 90 s for the O_2 and OI emissions, and 120 s for the comparatively weak Na emission layer were selected resulting in a cycle time of ~9 min for each emission except for the OI emission which was sampled twice per cycle. Because of the nature of the wave patterns imaged, it was often possible to measure wave motions with periods shorter than the sample rate by tracking the motion of nonuniformities in the wave forms (such as edges or "fronts") and inferring period from the measured wavelengths and phase speeds.

2.1.2. Image analysis. The image data have been analyzed to determine the horizontal wavelengths (λ) and observed phase speeds (v_h) of the waves evident in the data from which their observed periods (T_{ob}) and directions of motion were found. A variety of waves were measured during the ALOHA-93 campaign exhibiting horizontal wavelengths ranging from 10-54 km and phase speeds of up to ~100 m s^{-1} indicating relatively short observed periods in the range ~3 to 19 min. Details of these measurements (total 53 events) are given in a recent paper by M. J. Taylor et al. (Observed and intrinsic gravity wave parameters inferred from correlative nightglow imager and Na wind-temperature lidar observations at Haleakala, Maui, submitted to *Journal of Geophysical Research*, 1997a, hereinafter referred to as Taylor et al., submitted manuscript, 1997a). The four wave events selected for this study were most prominent in the OI (557.7 nm) emission (but on October 21 were also measured in the Na emission) and exhibited horizontal wavelengths in the range ~20-33 km and similar observed periods of 9.0 min (OI) on October 7, 8.9 min (Na) and 9.5 min (OI) on October 20, and 9.5 min (OI) on October 21. Table 1 details the measurements for these three nights. The azimuths of the wave motions observed on October 7 and 20 (~150°N) were similar but

differed significantly from the display recorded on October 21 which progressed toward the SW (azimuth ~235°).

Measurements of the intensity perturbations, $\langle I' \rangle / \langle \bar{I} \rangle$ (where $\langle \bar{I} \rangle$ represents the average intensity of the image, $\langle I' \rangle$ is a measure of the amplitude of the wave-induced intensity fluctuation, and the brackets denote that the observables represent an integral over the height of the emission region) induced by the passage of these waves through the OI and Na emission layers were determined by first flat-fielding the image data to remove the effects of lens vignetting and line of sight (van Rhijn) enhancement at low elevations. This was done for each event by constructing a "background" image by averaging together a series of typically 15-21 images centered on the image chosen for analysis. Prior to this the contributions of stars and electronic noise in each image were subtracted. A $\langle I' \rangle / \langle \bar{I} \rangle$ image was then created by dividing the data image by the background image and subtracting unity. This image was then "unwarped" to create a uniformly sampled map of the data suitable for spectral analysis (using an assumed height of 90 km for the Na data and 96 km for the OI data). For this study, determinations of $\langle I' \rangle / \langle \bar{I} \rangle$ were made by scanning across the relevant wave features present in the unwarped OI image. Mean values for each wave event were then found by averaging together several scans encompassing the wave field. Further details describing this method of analysis for measuring wave parameters and $\langle I' \rangle / \langle \bar{I} \rangle$ using airglow image data are given by *Garcia et al.* [1997]. This technique is a development on previous methods used to estimate $\langle I' \rangle / \langle \bar{I} \rangle$, which were mainly made in the vicinity of the zenith [e.g., *Hickey et al.*, 1997] and has the major advantage that measurements of the wave field are possible over any part of the all-sky image (which encompasses an area of $>0.6 \times 10^6$ km^2 at mesospheric heights). This method of analysis has been applied to the ALOHA-93 wave data and has yielded mean values of $\langle I' \rangle / \langle \bar{I} \rangle$ for the selected events of 4.6% (OI) on October 7, 5.9% (Na) and 6.7% (OI) on October 20 and 3% (OI) on October 21, with a typical measurement error of ±0.6% (see M. J. Taylor et al., Determination of fractional intensity variations induced by short period gravity waves using all-sky nightglow image data, submitted to *Journal of Geophysical Research*, 1997b, hereinafter referred to as Taylor et al., submitted manuscript, 1997b).

2.2. Haleakala Na Wind/Temperature Lidar Observations

During ALOHA-93 a Na wind/temperature (w/T) lidar was operated by the University of Illinois group from the summit of Haleakala at the Air Force Maui Optical Site. The 1 W laser, detector, and data acquisition system were interfaced with the 0.8 m diameter beam director telescope which provided full scanning capabilities for the lidar. During much of the campaign period the lidar was pointed at zenith (Z) and 15° off zenith to the north (N) and east (E) in the following sequence ZNZEZNZE. After compensating the signal for background noise and normalizing by the Rayleigh signal at 35 km altitude, the photon count data were used to generate profiles of Na density, temperature, and radial wind using the procedures described by *Gardner et al.* [1995] and *Tao and Gardner* [1995]. Temperature, vertical wind, and Na density profiles were obtained at the zenith position at a temporal resolution of ~7.5 min. Radial wind, temperature, and Na density profiles were obtained at the off zenith positions at a temporal resolution of ~15 min. The dominant error source is photon noise which is smallest at the Na layer peak and largest at the top and bottom edges of the layer where the Na density and hence lidar signal are smallest. When smoothed to 1 km and 30 min resolution, the total rms errors from all sources vary from approximately 1.9 K, 1.9 m s^{-1} (vertical wind), and 10 m s^{-1} (horizontal wind) at 85 and 100 km to 0.75 K, 0.75 m s^{-1} (vertical wind), and 4 m s^{-1} (horizontal wind) at 92 km.

The rms errors were estimated from a combination of approaches. We can estimate the photon noise errors directly from knowledge of the signal levels which vary with altitude. Errors caused by Na density perturbations, which also vary with altitude, must be estimated from knowledge of the gravity wave variance and the shape of the Na layer so that we can predict how much and how fast the density changes while we are making observations at the three different laser frequencies. Errors caused by frequency jitter of the laser can be estimated directly from the measured winds since a frequency error introduces a constant offset in winds or temperature at all altitudes. We simply look at the mean temperature profile and then compute the rms variation while noting that the frequency errors on different profiles are uncorrelated. All three estimates were combined by adding variances and taking the square root.

We describe the observed mean winds for each of the 3 days of interest separately. Values of mean winds were obtained by the Na w/T lidar approximately every 15 min. In order to avoid presenting numerous profiles, we have computed a mean wind profile for each night, as well as the standard deviation of all the wind profiles for a particular night. Averaging the wind profiles essentially removes the high-frequency fluctuating components, including gravity waves, and provides us with a better mean wind to use in our modeling.

When we average these winds for the approximately 5 hours observing period, any contribution from the semidiurnal winds will not average to zero. Therefore each altitude profile of the averaged background wind is dominated by the diurnal tide (as identified on the basis of the vertical wavelength), with some contribution expected from the semidiurnal tides (which are somewhat reduced in amplitude at this low latitude), long period gravity waves, and

Table 1. Observed Wave Parameters Derived From a Spectral Analysis of the OI (557.7 nm) Image Data and Estimates of the Wave Amplitude Ratios on October 7, 20, and 21, 1993

	λ_h, km	Period, min	Azimuth, deg	V_{ph}, m s^{-1}	$\langle \delta I \rangle / \langle \bar{I} \rangle$, %	Contrast, %
Wave A	20.0	9.0	150.0	36.9	4.6±0.6	9.2±1.2
Wave B	28.6	9.5	180 0	50.0	6.7±0.6	13.4±1.2
Wave C	30.1	9.5	210.0	52.8	5.7±0.6	11.4±1.2
Wave D	19.9	10.2	235.0	32.6	3.0±0.6	6.0±1.2

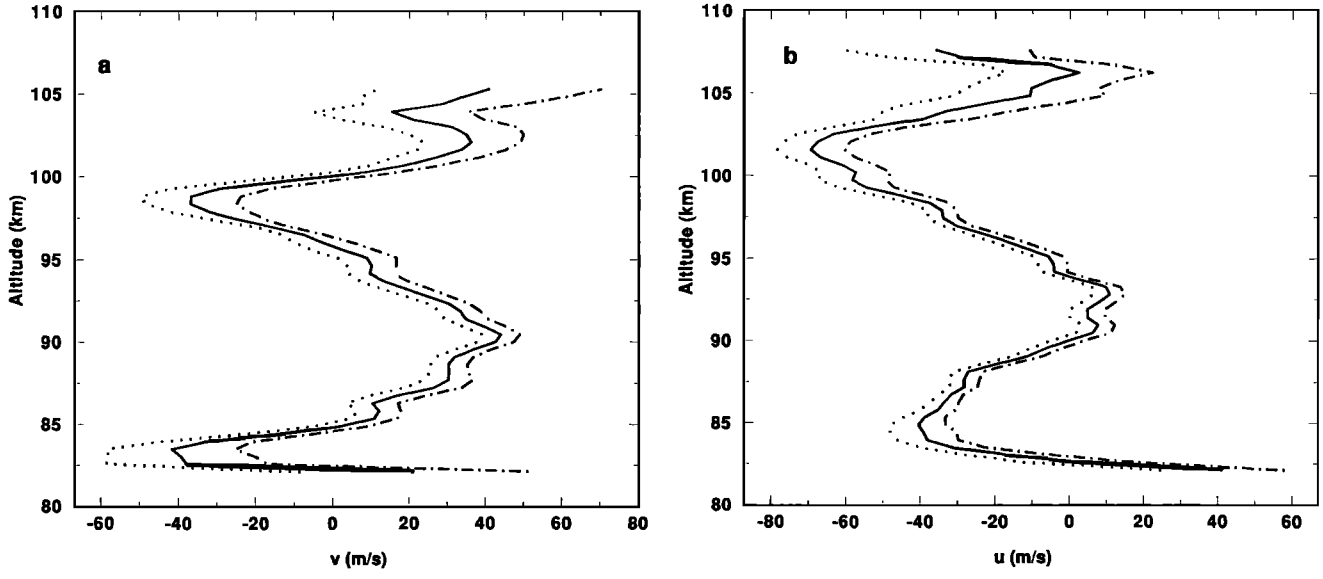

Figure 1. Mean (a) meridional (u) and (b) zonal (v) winds derived from the Na wind/temperature lidar observations for the night of October 7, 1993. Average profiles (solid curves) as well as the average plus 1 standard deviation (dotted curves) and minus 1 standard deviation (dash-dotted curves) are shown. The positive direction corresponds to due south in Figure 1a and due east in Figure 1b.

planetary waves. In our analysis there is no way for us to quantify these other contributions. The important requirement of this study is that we employ mean winds whose time variation is long compared to the gravity wave periods of interest. The approach we use to assess the validity of this is to examine the standard deviation of the wind profiles which provides a measure of the wind variability on a given night. If the standard deviation is much smaller than the mean, then we may conclude that low-frequency motions dominate. Our results will show that the standard deviation was always much smaller than the mean for the winds in the vicinity of the $O(^1S)$ emission layer.

The derived mean horizontal winds and their 1-σ limits (where σ is the standard deviation) are shown in Figures 1, 2, and 3 for the nights of October 7, 20, and 21, 1993, respectively. The meridional winds, v, and zonal winds, u, are shown between 83 and 106 km altitude, which covers the region of useful data for this analysis. For subsequent modeling purposes, these winds were represented analytically using the equation [*Lindzen*, 1970]

$$\bar{u}(z) = \frac{a_1}{2} z + \sum_i^N \delta_i \left(\frac{a_{i+1} - a_i}{2} \right) \ln \left[\frac{\cosh(z - z_i)/\delta_i}{\cosh z_i/\delta_i} \right] \quad (1)$$

The values of a_i, δ_i, z_i and N for the measured wind profiles are listed in Tables 2 to 4. Note that the last entry of the gradient (a_i) in these tables (equal to zero) produces a zero gradient (i.e., constant wind) at heights above the last entry of altitude (z_i) in the tables. The actual wind profiles used in our

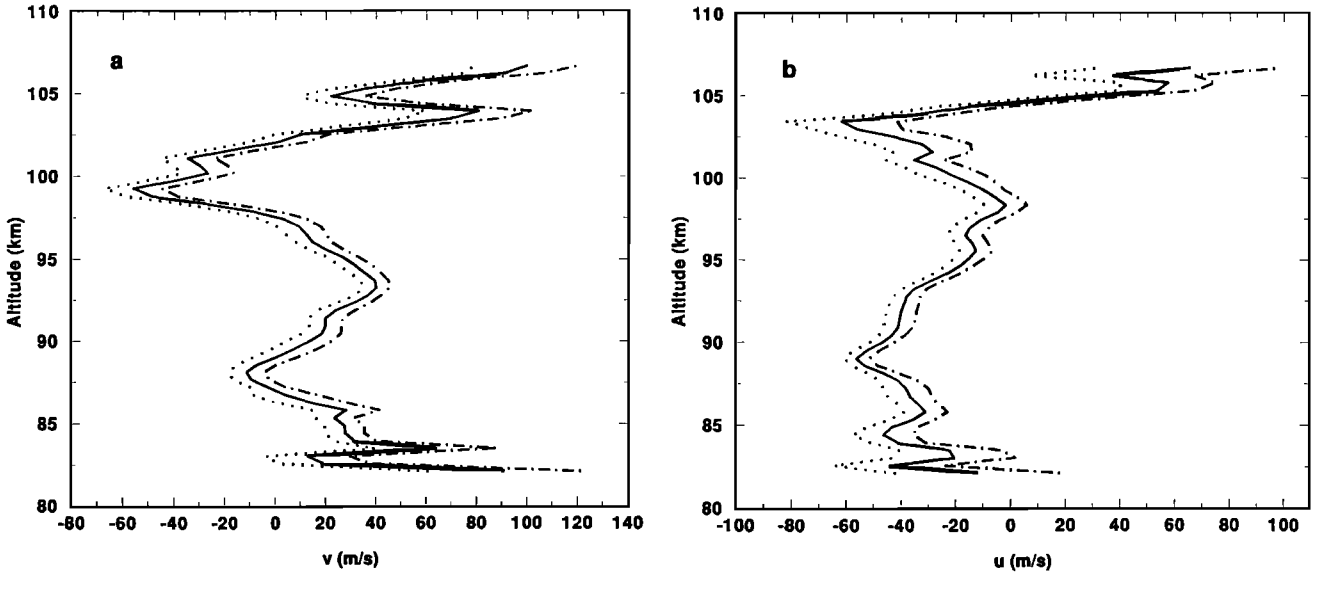

Figure 2. As in Figure 3, except for the night of October 20, 1993.

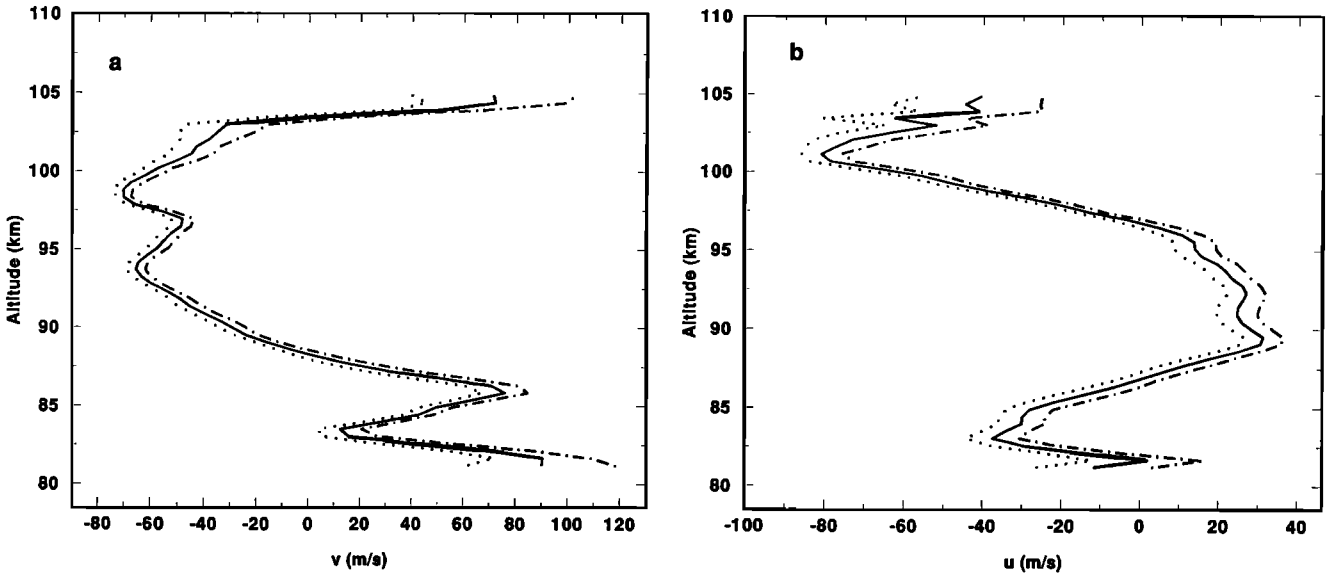

Figure 3. As in Figure 3, except for the night of October 21, 1993.

modeling are displayed and discussed in the results section. Note that here we employ a convention wherein meridional and zonal winds are positive if directed northward and eastward, respectively.

2.2.1. Mean Winds: October 7, 1993. A clear tidal structure with a vertical wavelength of about 14 km is evident in the w/T-lidar-derived meridional winds (Figure 1a). A similar feature is also seen in the mean zonal winds (Figure 1b), with a slightly larger vertical wavelength of 17 km. This structure is most probably due to the solar diurnal tide. The maximum northward and southward mean meridional winds are both about 40 m s^{-1}. The maximum westward wind of about 70 m s^{-1} occurs near 102 km, and the maximum eastward zonal wind is about 10 m s^{-1} near 93 km (except for the very large peak of about 40 m s^{-1} occurring at the lower altitude range of the data where the standard deviations are large). The mean zonal winds above about 83 km altitude are predominantly westward. The standard deviations typically lie between about 5 and 10 m s^{-1}, although near the lowest and highest operational altitudes of the lidar, they can exceed 20 m s^{-1}.

2.2.2. Mean Winds: October 20, 1993. Tidal structure is again evident in the mean winds (most probably due to the solar diurnal tide), and some smaller-scale features are also present. The meridional winds (Figure 2a) reveal structure with a vertical wavelength of about 11 km. The maximum southward wind of about 60 m s^{-1} occurs near 99 km altitude, while the maximum northward wind of about 100 m s^{-1} occurs near 106 km (where the standard deviations are large). The mean zonal winds (Figure 2b) are essentially westward at altitudes between about 84 and 104 km, with maximum westward velocities of almost 60 m s^{-1} occurring near 89 and

Table 2. Coefficients Used in Equation (1) to Represent the Na w/T Winds for the Night of October 7, 1993

	Meridional (N=11)			Zonal (N=18)		
i	a_i, s^{-1}	δ_i, km	z_i, km	a_i, s^{-1}	δ_i, km	z_i, km
1	0	1 0	80.00	0	1.0	80.00
2	-1.422×10^{-2}	0 5	82.11	2.132×10^{-2}	0.3	82.11
3	7.395×10^{-2}	0.5	83.30	-7.625×10^{-2}	1.0	82.57
4	$-3\ 365 \times 10^{-2}$	1.0	85.35	-6.164×10^{-2}	1.0	83.30
5	-7.651×10^{-3}	1 0	90.45	-1.714×10^{-2}	1.0	84.00
6	9.684×10^{-3}	1.0	94.60	4.889×10^{-3}	1.0	88.50
7	1.424×10^{-2}	1.0	98.80	2.200×10^{-2}	1 0	90.00
8	-2.892×10^{-2}	0.5	102.05	$1\ 000 \times 10^{-3}$	1.0	94.00
9	1.838×10^{-2}	0.5	103.90	-4.000×10^{-2}	1.0	94.50
10	-3.237×10^{-2}	1.0	105.29	-2.667×10^{-3}	1.0	96.00
11	1.168×10^{-2}	1.0	110.00	-1.400×10^{-2}	1.0	98.00
12	0	--	--	-1.000×10^{-2}	1.0	99.00
13	--	--	--	$-1\ 000 \times 10^{-2}$	1.0	100.50
14	--	--	--	-6.667×10^{-3}	1.0	102.30
15	--	--	--	3.353×10^{-2}	1.0	104.00
16	--	--	--	1.351×10^{-2}	0.5	106.22
17	--	--	--	-3.597×10^{-2}	0.2	107.61
18	--	--	--	1.674×10^{-2}	1.0	110.00
19	--	--	--	0	--	--

Table 3. Coefficients Used in Equation (1) to Represent the Na w/T Winds for the Night of October 20, 1993

	Meridional (N=19)			Zonal (N=15)		
i	a_i, s^{-1}	δ_i, km	z_i, km	a_i, s^{-1}	δ_i, km	z_i, km
1	0	1.0	80.00	0	1.0	80.00
2	-4.502×10^{-2}	0.2	82.11	-5.687×10^{-3}	0.5	82.11
3	1.129×10^{-1}	0.2	83.04	-2.008×10^{-2}	1.0	84.50
4	-1.739×10^{-1}	0.2	83.50	2.909×10^{-2}	0.5	85.60
5	3.094×10^{-2}	0.2	84.89	-6.000×10^{-3}	0.5	87.60
6	-1.311×10^{-2}	0.5	85.50	-1.533×10^{-2}	0.5	89.10
7	2.400×10^{-2}	1.0	88.00	2.222×10^{-2}	0.5	90.00
8	-1.840×10^{-2}	1.0	90.50	1.786×10^{-3}	0.5	92.80
9	-6.667×10^{-4}	1.0	92.00	1.045×10^{-2}	0.5	95.00
10	-2.400×10^{-2}	1.0	93.25	8.000×10^{-4}	0.5	97.50
11	1.527×10^{-2}	1.0	96.00	2.400×10^{-2}	0.5	98.25
12	5.000×10^{-3}	1.0	98.00	-1.268×10^{-2}	0.5	101.80
13	5.200×10^{-2}	0.2	99.25	-1.707×10^{-2}	0.5	103.44
14	-6.000×10^{-2}	0.2	100.00	5.862×10^{-2}	0.5	105.76
15	1.200×10^{-2}	0.2	101.25	-1.604×10^{-2}	0.5	110.00
16	-4.528×10^{-2}	0.2	103.90	0	--	--
17	7.312×10^{-2}	0.2	104.83	--	--	--
18	-4.757×10^{-2}	0.2	106.68	--	--	--
19	3.163×10^{-2}	1.0	110.00	--	--	--
20	0	--	--	--	--	--

104 km altitude. This suggests a vertical wavelength of almost 15 km. Above about 104 km the zonal winds reverse, achieving eastward velocities of 60 m s^{-1}. Above about 103 km and below about 84 km the standard deviations become large (~20 m s^{-1}). Between these two altitudes the standard deviations are typically less than 10 m s^{-1}.

2.2.3. Mean Winds: October 21, 1993. The mean winds of October 21 have a tidal structure that is quite different to that of the other two nights. The lidar data from this night have been analyzed by *Dao et al.* [1995], who suggest that the structure is most probably due to the diurnal tide. The apparent vertical wavelength of this tidal structure is about 20 km (Figure 3a). (Note that the true vertical wavelength may be different from this value because above about 103 km altitude the winds have a poorer statistical significance than those at lower altitudes, thus complicating the determination of the vertical wavelength. Obtaining the tidal vertical wavelength from the zonal winds (Figure 3b) is not feasible in this instance.)

Above 88 km altitude the mean meridional wind is southward, achieving a maximum southward velocity of 70 m s^{-1} just above 98 km. The maximum wind in the northward direction of 75 m s^{-1} occurs near 86 km altitude (those occurring at the extreme upper and lower altitude ranges of the data being less statistically significant). Between about 87 and 97 km the mean zonal winds are directed eastward, achieving a maximum of about 30 m s^{-1} near 89 km. The minimum zonal wind (-80 m s^{-1}) occurs near 103 km.

Table 4. Coefficients Used in Equation (1) to Represent the Na w/T Winds for the Night of October 21, 1993.

	Meridional (N=12)			Zonal (N=17)		
i	a_i, s^{-1}	δ_i, km	z_i, km	a_i, s^{-1}	δ_i, km	z_i, km
1	0	1.0	75.00	0	1.0	80.00
2	-1.504×10^{-2}	0.5	81.65	1.212×10^{-3}	0.5	81.65
3	6.364×10^{-2}	0.5	83.30	-3.696×10^{-2}	0.5	82.11
4	-3.656×10^{-2}	0.5	85.82	-3.226×10^{-2}	0.5	83.04
5	3.233×10^{-2}	0.2	89 25	1.848×10^{-2}	0.5	83.96
6	1.024×10^{-2}	0.5	93.60	-2.151×10^{-3}	0.5	84.89
7	-6.890×10^{-3}	0.5	97.25	1.454×10^{-2}	0.5	89.43
8	2.568×10^{-2}	0.5	98.50	-9.396×10^{-3}	0.5	90.92
9	-9.796×10^{-3}	0.2	102.97	4.317×10^{-3}	0.5	92.31
10	-6.451×10^{-2}	0.2	103.44	-5.396×10^{-3}	0.5	95.09
11	-5.749×10^{-2}	0.2	104.80	-1.075×10^{-3}	0.5	96.02
12	1.481×10^{-2}	0.2	110.00	-1.931×10^{-2}	0.5	101.20
13	0	--	--	2.147×10^{-2}	0.2	102.97
14	--	--	--	-3.191×10^{-2}	0.2	103.44
15	--	--	--	5.000×10^{-2}	0.2	103.90
16	--	--	--	1.075×10^{-3}	0.2	104.83
17	--	--	--	7.930×10^{-3}	0.5	110.0
18	--	--	--	0	--	--

3. Full-Wave Model

The gravity wave model is a robust, one-dimensional, time-independent full-wave model describing the propagation of nonhydrostatic, linear gravity waves from the ground up to a maximum altitude of 500 km [*Hickey et al.*, 1994, 1995, 1997]. It includes dissipation due to eddy processes in the lower atmosphere and molecular processes (viscosity, thermal conduction, and ion-drag) in the upper atmosphere. Height variations of the mean temperature and horizontal winds, as well as Coriolis force are all included. The model therefore accurately describes the propagation of gravity waves in an inhomogeneous atmosphere.

The equations that we solve are the continuity equation (2), the Navier-Stokes equations (3), the energy equation (4), and the ideal gas equation (5). These equations are linearized and used to describe fully compressible one-dimensional waves. In our full-wave model coordinate system, x is positive due south, y is positive due east, and z is positive upward. The equations are

$$D\rho/Dt + \rho\underline{\nabla}.\underline{v} = 0 \tag{2}$$

$$\rho\frac{D\underline{v}}{Dt} + \underline{\nabla}p - \rho\underline{g} + 2\rho\underline{\Omega}\mathrm{x}\underline{v} + \underline{\nabla}.\underline{\underline{\sigma}}_m + \underline{\nabla}.\left(\rho\eta_e\underline{\nabla}\underline{v}\right) + \rho\nu_{ni}\left(\underline{v} - \underline{v}_i\right) = \underline{0} \tag{3}$$

$$c_v\rho\frac{DT}{Dt} + p\underline{\nabla}.\underline{v} + \underline{\underline{\sigma}}_m:\underline{\nabla}\underline{v} - \underline{\nabla}.\left(\lambda_m\underline{\nabla}T\right) - \frac{c_v T}{\theta}\underline{\nabla}.\left[\rho\kappa_e\underline{\nabla}\theta\right] + \rho\nu_{ni}\left(\underline{v} - \underline{v}_i\right)^2 = 0 \tag{4}$$

$$p = \rho RT/M \tag{5}$$

where $\underline{v}$ is the velocity with x, y, z components u, v and w, respectively; ρ is the neutral mass density; p is atmospheric pressure; g is the gravitational acceleration; $\underline{\Omega}$ is the Earth's angular velocity; $\underline{\underline{\sigma}}_m$ is the molecular viscous stress tensor; η_e is the eddy momentum diffusivity; ν_{ni} is the neutral-ion collision frequency; $\underline{v}_i$ is the ion velocity; c_v is the specific heat at constant volume; T is temperature; λ_m is the molecular thermal conductivity; θ is the potential temperature ($\theta = T(p_0/p)^{R/c_p}$, where p_0 = 1000 mbar, c_p is the specific heat at constant pressure, and R is the gas constant); κ_e is the eddy thermal diffusivity; and M is the mean molecular weight. The operator $D/Dt = \partial/\partial t + \underline{v}\cdot\underline{\nabla}$ is the substantial derivative, where $\underline{v}(z)$ is the total wind (mean plus perturbation). Note that in *Hickey et al.* [1997] the substantial derivative was inadvertently and incorrectly written as $D/Dt = \partial/\partial t + \underline{v}_0\cdot\underline{\nabla}$, where $\underline{v}_0$ is the mean velocity.

The linear wave solutions to these equations are assumed to vary as exp i(ωt-kx-ly), where ω is the wave frequency and k and l are the horizontal wavenumbers in the x (meridional) and y (zonal) directions, respectively. The form of these solutions assumes that the mean state varies neither in time nor in the horizontal direction. The six linearized equations are reduced to five by eliminating the density perturbation using the linearized ideal gas equation. The remaining five equations are second-order, ordinary differential equations in the vertical coordinate z. This coupled system of equations is solved subject to boundary conditions for the wave variables u', v', w' (the meridional, zonal, and vertical velocity perturbations, respectively), T' and p' (the temperature and pressure perturbations, respectively). First, these variables (Ψ) are transformed to new variables (Ψ^*) by dividing by the square root of the mean atmospheric density, $\bar{\rho}$ (i.e., $\psi^* = \psi/\bar{\rho}^{1/2}$). We solve for the transformed variables by expressing vertical derivatives as centered finite differences and then using the tridiagonal algorithm [*Bruce et al.*, 1953] to solve the resulting set of difference equations subject to boundary conditions. The untransformed lower boundary condition is $w' = 0$, and vertical gradients in u', v', T', and p' are defined based on the equations for an adiabatic and isothermal atmosphere. At the upper boundary the radiation condition is applied, using the WKB solution described by *Hickey and Cole* [1987]. The upper boundary is chosen to be high enough so that wave reflection from the upper boundary will not influence results at lower altitudes in the model (this was implemented by adjusting the upper boundary height until a WKB wave experiences severe damping within a timescale of one wave period). A Gaussian profile of half width 1.5 km and centered near the tropopause is used to provide the wave forcing. The final wave variables are obtained by a simple inverse transformation. The finite difference equations in the region between the lower boundary (ground) and the upper boundary (the latter lying between 200 and 500 km) are represented on a grid of 18,000 points with a vertical resolution of 11 to 28 m.

The model outputs the wave variables u', v', w', T', and p' given the wave frequency (ω), the horizontal wavelength (λ), and the azimuth of propagation (φ). Mean state quantities required for the full-wave computations are nominally provided by the mass spectrometer and incoherent scatter (MSIS-90) model [*Hedin*, 1991]. The molecular coefficients of viscosity and thermal conductivity are taken from *Rees* [1989]. The eddy momentum diffusivity increases exponentially from 0.1 $m^2\ s^{-1}$ at the ground to a maximum value of about 300 $m^2\ s^{-1}$ at 80 km altitude, and decreases exponentially above that to an insignificant value near 140 km altitude. This eddy diffusion profile approximates that given by *Strobel* [1989]. The eddy thermal diffusivity is calculated from the eddy momentum diffusivity by assuming a Prandtl number of 3 [see *Strobel*, 1989].

3.1. O(^1S) Airglow Fluctuation Model

The response of nightglow emissions to gravity wave forcing has been described before [see *Hickey et al.*, 1997, and references therein]. For each of the minor species involved in a particular emission chemistry the linearized continuity equation can be written as:

$$i\omega n' = \delta P - \delta L + \mathrm{w}'\frac{\partial\bar{n}}{\partial z} - \underline{\nabla}\cdot\underline{v}'\bar{n} \tag{6}$$

where δP and δL are the perturbations in the chemical production and loss, respectively; n' is the minor species number density perturbation about its mean value, $\bar{n}$; w' is the gravity wave vertical velocity component; and $\underline{\nabla}\cdot\underline{v}'$ is the gravity wave velocity divergence. The perturbations in chemical production and loss (δP and δL) are due to perturbations in temperature (for temperature-dependent reactions), perturbations in the major gas density (for three-body recombination reactions), and are also due to chemical

coupling between reacting minor species. Prior to the study of *Hickey et al.* [1997], the gravity wave perturbations in the vertical velocity, velocity divergence, temperature, and major gas density were calculated using our WKB models [e.g., *Schubert and Walterscheid*, 1988; *Schubert et al.*, 1991; *Hickey et al.*, 1993a, b]. Here, as in the work of *Hickey et al.* [1997], we use the full-wave model described in section 3 and by *Hickey et al.* [1994, 1995, 1997] to calculate these wave perturbations.

The fact that the nightglow emission intensity I is proportional to the density n of the emitting species allows us to write $\delta I / \bar{I} = \delta n / \bar{n}$. The imager collects photons that originate from all altitudes within the nightglow emission layer. Therefore, in order to simulate the airglow images, the airglow response to the gravity wave was integrated over the complete vertical extent of the airglow layer. The integration covered the altitude interval between 75 and 130 km. The amplitude of the modeled gravity wave is then adjusted so that the modeled relative intensity fluctuation, $\langle \delta I \rangle / \langle \bar{I} \rangle$, compares with the measured value, thus providing an estimate of the wave amplitude (here the angle brackets denote an altitude integral). The chemical scheme that we employ to describe the production of the $O(^1S)$ emission in the mesopause region as well as the pertinent reaction rates and efficiencies are given in the appendix.

The gravity wave forcing on the minor species concentrations is specified by the perturbation variables $T'/\bar{T}$, $\underline{\nabla} \cdot \underline{v}'$, w' and $n'(M)/\bar{n}(M)$ output by the full-wave model. A set of complex dynamical factors derived from these perturbation variables and defined by equations (A6) to (A8) are then substituted into algebraic expressions describing the minor species fluctuations (equations (A3) to (A6)). The mean state densities of $O_2(c^1\Sigma_u^-)$ and $O(^1S)$ are calculated using equations (A1) and (A2). The only other parameters required to solve for n' in (1) are those defining the undisturbed state of the atomic oxygen profile (and its vertical derivative). We employ the undisturbed atomic oxygen density profile derived from the MSIS-90 model of *Hedin* [1991]. The atomic oxygen concentration and the $O(^1S)$ undisturbed emission intensity resulting from the chemical scheme described in the appendix are shown in Figure A1. The $O(^1S)$ emission layer peaks near 93.5 km with a full-width half-maximum of about 5 km.

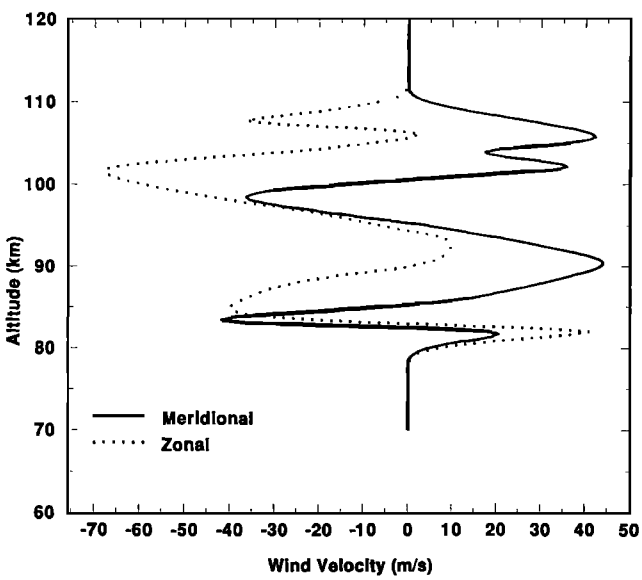

Figure 4. Mean wind profiles employed in the computations derived by fitting the analytic function given by equation (1) in the text to the measured winds of Figure 2 for the night of October 7, 1993. The fitting parameters are provided in Table 2.

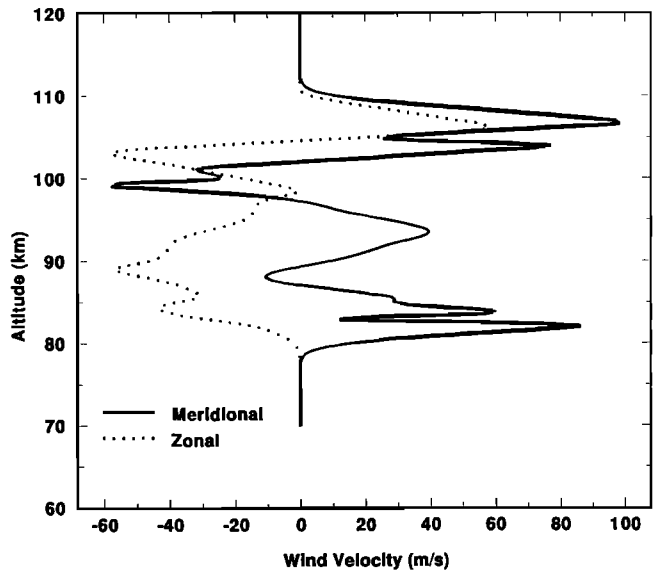

Figure 5. Same as in Figure 5, except for the night of October 20, 1993 with the fitting parameters provided in Table 3.

4. Results

The waves studied here have horizontal phase speeds ranging from about 33 to 53 m s^{-1}, making them susceptible to the effects of Doppler shifting associated with the mean winds. Our simulations were performed using the winds measured by the Na w/T lidar, as discussed in section 2.2, and as represented in our model using equation (1) with the coefficients given in Tables 2-4. For modeling purposes, the mean wind values were smoothly decreased to zero below 83 km altitude and above 106 km altitude. This is not expected to modify our gravity wave results in the vicinity of the $O(^1S)$ emission peak. We investigated the effects of smoothly decreasing the wind values to zero at other altitudes (e.g., 70 km), as well as keeping the winds constant and nonzero above 106 km. In all cases the results remained essentially unchanged. The actual wind profiles employed in our simulations are shown in Figures 4, 5, and 6.

The values of wave amplitude derived from our simulations were usually quite modest, but occasionally over limited height ranges they were large enough to render the wave unstable based on standard convective instability criteria. The criterion for wave instability is that the wave velocity amplitude exceed the wave phase speed [*Orlanski and Bryan*, 1969; *Lindzen*, 1981; *Fritts*, 1984; *Walterscheid and Schubert*, 1990]. Alternatively, a wave becomes convectively unstable when the vertical derivative of the total (mean plus wave) potential temperature (θ) just becomes negative. Note that the numerical simulations of *Walterscheid and Schubert* [1990] and *Andreassen et al.* [1994] suggest

that some overshoot is possible, whereby wave amplitudes may become somewhat larger than those implied from simple stability analysis. In the results that follow, we plot the wave temperature amplitude as a function of altitude that gives a relative intensity perturbation equal to the observed value. If the temperature amplitude exceeds its maximum permitted stable temperature amplitude over a limited altitude range (based on the second instability criterion described above), we also indicate on the figure and for this limited altitude range only the maximum permitted stable temperature amplitude.

Results are presented separately for the four waves. We present results for altitudes between 30 and 110 km, in spite of the fact that the model is somewhat unconstrained outside the range of the available lidar wind data (~83 to 105 km). We do so at the higher altitudes only to emphasize the differences between the wave propagation into the thermosphere, while noting that the results we obtain at 110 km are dependent on the assumed mean winds there. We present results below 80 km in order to clearly show the general growth of wave amplitude with increasing height, and to elucidate some of the key physical processes that can accompany wave propagation through the atmosphere (such as wave reflection and standing wave behavior). The results presented for this lower atmospheric region are again dependent on the assumed mean winds there. The assumption of a zero mean wind in the lower atmosphere is not of a major concern, however, because at these altitudes mean wind amplitudes (including contributions from tidal and planetary waves) are not expected to be large.

Because we employ the MSIS-90 model [*Hedin*, 1991] to define the basic undisturbed state of the atmosphere, we require the solar and geomagnetic inputs relevant to the times of the observations. The daily values of $F_{10.7}$ (with the daily planetary magnetic index, A_p, given in parentheses) were 116.6 (3), 93.5 (4), and 94.2 (5) for October 7, 20, and 21, respectively. The differences that these inputs make to the empirically determined mesospheric mean state are not significant to this study (the upper thermosphere is significantly affected by the different geophysical inputs, but this is not relevant to the present study).

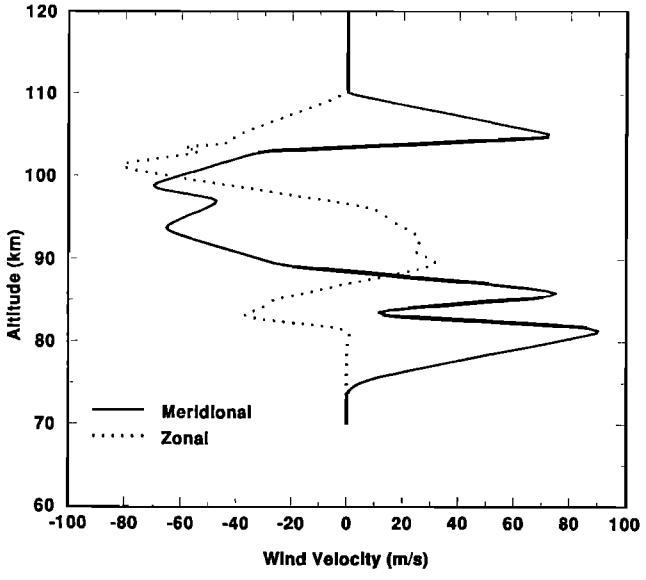

Figure 6. Same as in Figure 5, except for the night of October 21, 1993 with the fitting parameters provided in Table 4.

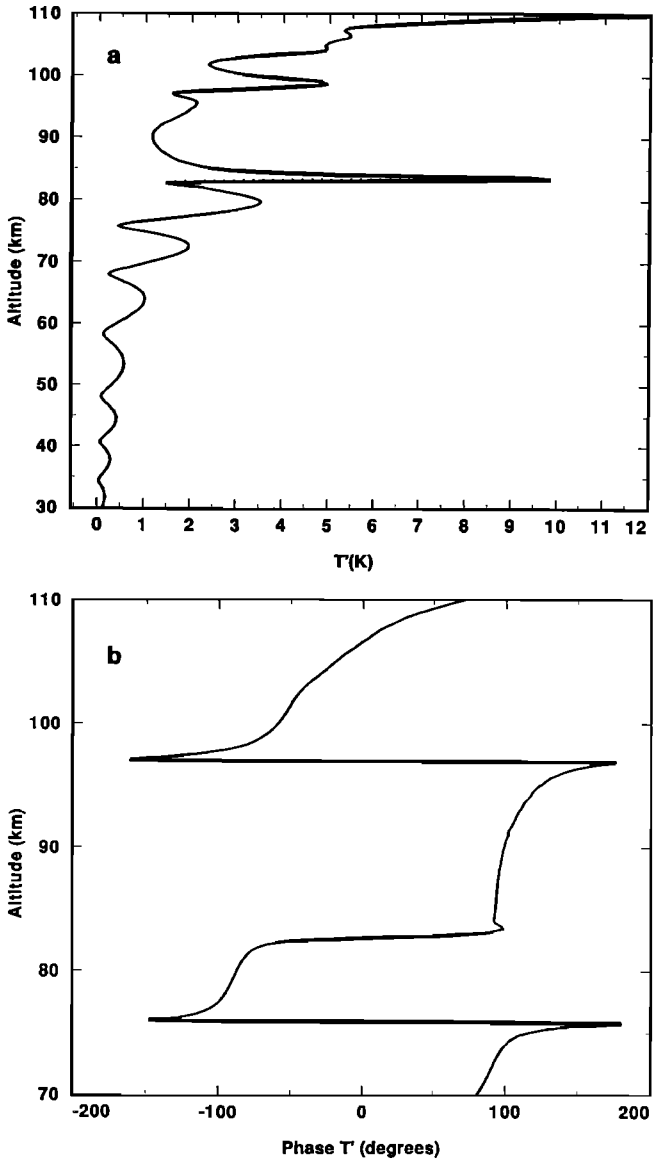

Figure 7. Wave A temperature perturbation amplitude required to reproduce the observed relative intensity perturbation measured by the all-sky imager on October 7, 1993: (a) T' and (b) phase T'.

4.1. Wave A

The results for the wave observed on October 7, 1993 are shown in Figure 7. Between about 80 and 83 km altitude the derived wave amplitudes slightly exceed their maximum allowed values based on our adopted stability criterion, and the maximum wave amplitude in this region is about 10 K (Figure 7a). These large wave amplitudes arise as a consequence of strong Doppler shifting of the wave frequency to small values by the mean winds in this region. The mean winds do not Doppler shift the wave frequency to zero (i.e., there is no critical level), but the mean wind shears are large in this region (where the local Richardson number,

Ri, is less than 0.25, and where $Ri = N^2/(\partial u^*/\partial z)^2$, N is the local Brunt-Vaisala frequency, and the horizontal wind shear is $\partial u^*/\partial z$ where u^* is the component of the mean wind in the direction of phase propagation). As this altitude is approached from below, the aspect ratio of the wave decreases, the horizontal and vertical velocity perturbations increase and decrease, respectively, and the temperature perturbation initially increases in order to conserve wave action [*Bretherton and Garrett*, 1968]. Close to the level of minimum intrinsic frequency the dissipation of the wave becomes severe because the wave intrinsic phase speed has become very small, and a sharp reduction in wave amplitude occurs (near 82.5 km). Above this level the wave intrinsic phase speed increases with increasing altitude, the dissipation rate decreases, and the temperature perturbation amplitude increases again in order to conserve wave action. At slightly greater altitudes where the wave leaves the region of strong Doppler shifting the aspect ratio of the wave returns to its (approximate) initial value, and the temperature perturbation amplitude of the wave decreases appropriately. Because the region of strong Doppler shifting is narrow (~1 km) compared to the vertical wavelength of the wave (several kilometers), the loss of wave (action) amplitude as a result of the encounter is not severe. This can be seen by comparing the wave amplitudes below (near 80 km) and above (near 85 km) the 83 km level.

Wave amplitude decreases from about 8 K near 80 km to about 0.5 K near 30 km. Strong partial reflections, producing quasi-standing wave behavior, are noted in the derived wave amplitudes below about 80 km. (This standing wave behavior was inferred from examination of the phase difference between the vertical velocity perturbation, w', and the pressure perturbation, p'. Standing waves produced by strong reflections will have no vertical component of energy flux, and so w' and p' will be in phase quadrature. In the present case their phase difference was about 70^o below 80 km.) Above about 103 km the derived wave amplitudes increase approximately linearly with increasing altitude. In this lower thermosphere region the mean, undisturbed temperature increases uniformly with increasing altitude, so that the ratio T'/T remains approximately constant. Above about 105 km, where we have no knowledge of the mean winds, our model is completely unconstrained and the results are questionable. However, the wave is fast enough (37 m s^{-1}) to survive propagation to 130 km altitude without significant viscous dissipation if mean winds are ignored at these altitudes.

Between about 83 and 103 km altitude the derived wave amplitudes are typically 2 K. A pronounced local maximum in T' occurs near 98 km altitude, with an amplitude of about 6 K. Over this same altitude range the vertical wavelength (Figure 7b) slightly exceeds 20 km. There are two regions where the mean winds Doppler shift the wave frequency to higher frequencies. One lies between about 85 and 95 km and the other lies between about 100 and 105 km. In these regions the wave becomes locally evanescent, explaining the large vertical wavelength over much of the $O(^1S)$ emission layer. This implies that phase variations of perturbation quantities are small over much of the $O(^1S)$ emission layer (which peaks near 97 km) and that consequently the effects of destructive interference between intensity fluctuations occurring at different altitude levels within the emission layer are minimal.

4.2. Wave B

The results for this wave observed on October 20, 1993 are shown in Figure 8. Between about 96 and 99 km altitude (i.e., in the vicinity of the peak of the $O(^1S)$ emission) the derived wave amplitudes (shown in Figure 8a) exceed their maximum allowed values based on our adopted stability criterion. The maximum wave amplitude is about 16 K near 98 km. The phase of T' (Figure 8b) undergoes a rapid variation between about 97 and 100 km altitude, implying a very small vertical wavelength in this region. The wave encounters a critical level near 99 km altitude, which causes the temperature perturbation to increase just below the critical level due to the effects of the mean winds as discussed in the previous section. Because the Richardson number calculated on the

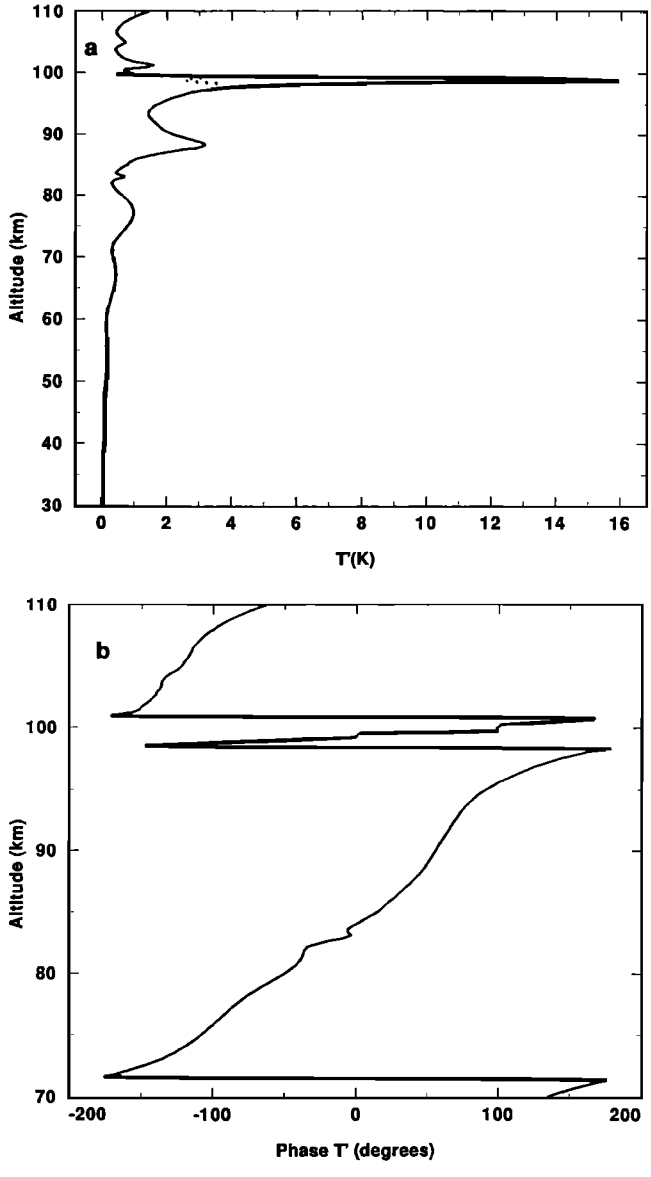

Figure 8. Wave B temperature perturbation amplitude required to reproduce the observed relative intensity perturbation measured by the all-sky imager on October 20, 1993. The dotted curve shows the limiting amplitude determined from the convective instability criterion discussed in the text: (a) T' and (b) phase T'.

basis of the background wind alone at the critical level is about 0.25, the wave is able to propagate through the critical level with little attenuation [see, e.g., *Breeding*, 1971]. Note that in this analysis the Richardson number is calculated using the mean winds only, and any contribution from the waves is not considered.

Above about 100 km the derived wave amplitudes remain small (less than about 2 K) and approximately constant with altitude. Because the mean, undisturbed temperature increases uniformly and quite rapidly above about 100 km, the ratio $T'/\bar{T}$ must be decreasing with increasing altitude above 100 km. Therefore the propagation of this wave above 100 km altitude is somewhat inhibited. At altitudes above 106 km our mean wind information is nil, and we assume that the mean winds smoothly approach zero near 110 km. An accurate description of the behavior of the wave above about 106 km altitude is therefore not possible, but our results indicate that near 110 km altitude the wave perturbation is small.

Below about 97 km the derived wave amplitudes generally decrease with decreasing altitude except for the slight increases associated with local maxima due to the effects of partial reflections. At 30 km altitude the temperature perturbation amplitude is very small (a fraction of a degree).

4.3. Wave C

This wave is one of two observed in the O(^1S) nightglow emission on October 21, 1993. The results are shown in Figure 9. Between about 92 and 95 km the wave amplitude (Figure 9a) exceeds its maximum allowed values based on our adopted stability criterion. The maximum wave amplitude of about 11 K occurs near 93.5 km altitude. This local temperature perturbation maximum near 93.5 km is not associated with a critical level, but it is due to the effects of Doppler shifting of the wave frequency by the mean winds. A local maximum in the intrinsic period (of about 80 min) occurs near 93.5 km, and in a similar fashion to the critical level encounter discussed previously for wave B, the temperature perturbation increases in order to conserve wave action. This wave encounters two critical levels, one near 97.5 km and the other near 102.5 km. The Richardson number at these two levels exceeds unity, and as theory predicts [e.g., *Breeding*, 1971], the attenuation of the wave through the critical level is large. Between about 91 and 102.5 km the intrinsic wave period never falls below about 20 min, so that the intrinsic phase speed is about 60% of that given in Table 1. This increases the effects of dissipation, and this wave is severely attenuated above about 97 km altitude. Between about 97 and 98 km altitude the wave amplitude decreases linearly from about 3 K to about 0.1 K. Therefore these results show that the observed O(^1S) emission fluctuations are primarily the result of gravity wave fluctuations occurring on the underside of the O(^1S) emission layer. The phase of T' (Figure 9b) shows that the vertical wavelength varies from about 7 km on the underside of the O(^1S) emission layer to about 2 km near the emission peak.

This wave is essentially unable to propagate above about 99 km altitude (Figure 9a). Below about 93 km altitude the wave amplitudes decrease with decreasing altitude except for the slight increases associated with the effects of weak partial reflections. At 30 km altitude the wave amplitude is small (a fraction of a degree).

4.4. Wave D

This is the second wave observed in the O(^1S) nightglow emission on October 21, 1993. The results are shown in Figure 10. The azimuth of propagation for this wave (235°) is similar to that of wave C (210°), but this wave has a smaller phase speed (32.6 m s^{-1}) than wave C (52.8 m s^{-1}). Consequently, it is not surprising that the results for waves C and D are similar because the two waves are quite similar and propagate through identical mean winds. Between about 93 and 97 km the wave amplitude (Figure 10a) exceeds its maximum allowed values based on our adopted stability criterion. The maximum wave amplitude of about 7 K occurs near 94 km altitude. Between about 97 and 98 km altitude the wave amplitude decreases linearly from about 5 K to about

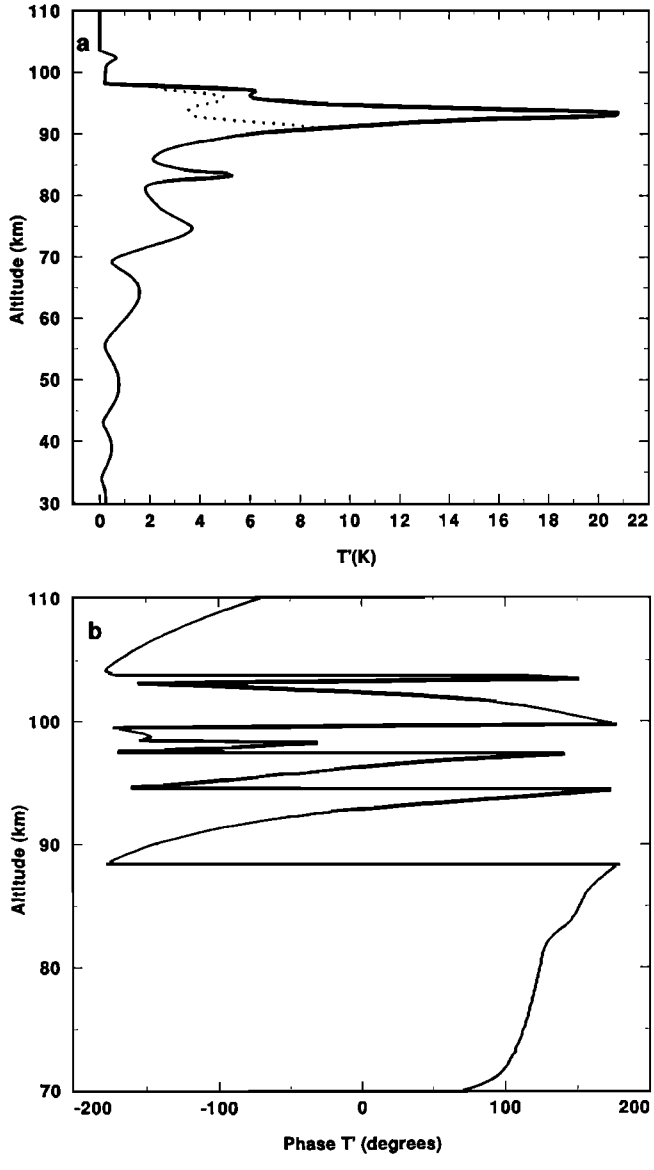

Figure 9. Wave C temperature perturbation amplitude required to reproduce the observed relative intensity perturbation measured by all-sky the imager on October 21, 1993. The dotted curve shows the limiting amplitude determined from the convective instability criterion discussed in the text: (a) T' and (b) phase T'.

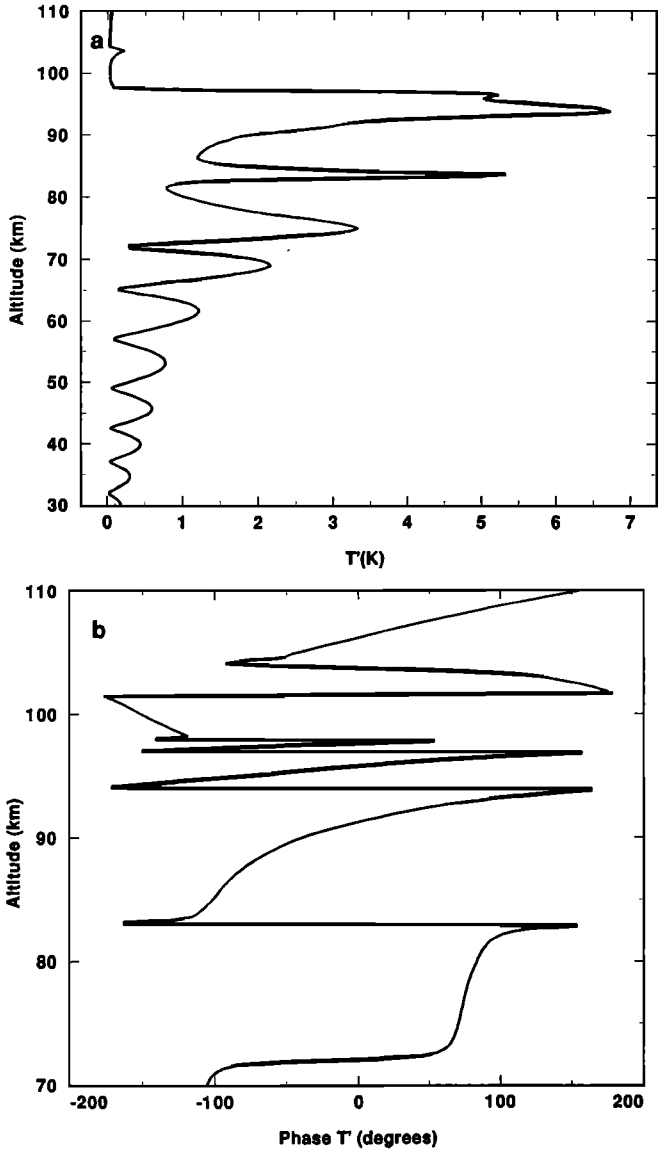

Figure 10. Wave D temperature perturbation amplitude required to reproduce the observed relative intensity perturbation measured by the all-sky imager on October 21, 1993. The dotted curve shows the limiting amplitude determined from the convective instability criterion discussed in the text: (a) T' and (b) phase T'.

0.1 K. Therefore, like those of wave C, these results show that the observed O(^1S) emission fluctuations are primarily the result of gravity wave fluctuations occurring on the underside of the O(^1S) emission layer. The phase of T' (Figure 10b) shows that the vertical wavelength varies from about 10 km on the underside of the O(^1S) emission layer to about 4 km near the emission peak.

This wave (like wave C) encounters two critical levels, one near 97 km and the other near 103 km. In the vicinity of these critical levels the intrinsic wave period always exceeds about 20 min, increasing the dissipation of this wave in this region (as for wave C). Because this wave (D) has a smaller extrinsic phase speed than that of wave C (32.6 m s^{-1} versus 52.8 m s^{-1}), the effects of the mean winds are stronger for wave D. The intrinsic phase speed of wave D is smaller than that of wave C between about 93 and 103 km, and the dissipation rate of wave D is consequently greater than that of wave C. This wave is essentially unable to propagate above about 98 km altitude (Figure 10a) because the Richardson number exceeds unity at the critical level and, as theory predicts [e.g., *Breeding*, 1971], the attenuation of the wave through the critical level is large. Below about 93.5 km altitude the wave amplitudes generally decrease with decreasing altitude. The partial reflections are much stronger for this wave that for the previous three. At 30 km altitude the wave amplitude is small (a fraction of a degree).

4.5. Results Summary

The simulated temperature perturbation amplitudes for the four waves are summarized in Figure 11. Clearly, wave A is able to easily propagate to the 110 km level and can propagate much higher than this (~130 km) if the mean winds are negligible above about 110 km. The propagation of wave B into the thermosphere is somewhat restricted. Waves C and D are both unable to propagate above about 97 km altitude. The values of the Richardson number at the critical levels (Ri_c) appear to affect the transmission of the waves through the critical levels, as theory predicts [e.g., *Breeding*, 1971]. In the case of wave B, Ri_c is about 0.25 (and the wave is essentially transmitted through the critical level), whereas in the case of waves C and D, Ri_c exceeds unity (and the waves are attenuated at the critical level). These results demonstrate the importance of mean wind filtering of gravity waves, and how mean winds affect the wave-coupling between different atmospheric regions.

5. Discussion

Three of the waves studied encountered critical levels in the mesopause region as a consequence of the large mean winds. Wave A encountered a region near 82.5 km (which is well below the O(^1S) emission layer) where the mean winds caused a strong Doppler shifting of the wave frequency to small values. The wave was not severely attenuated by this

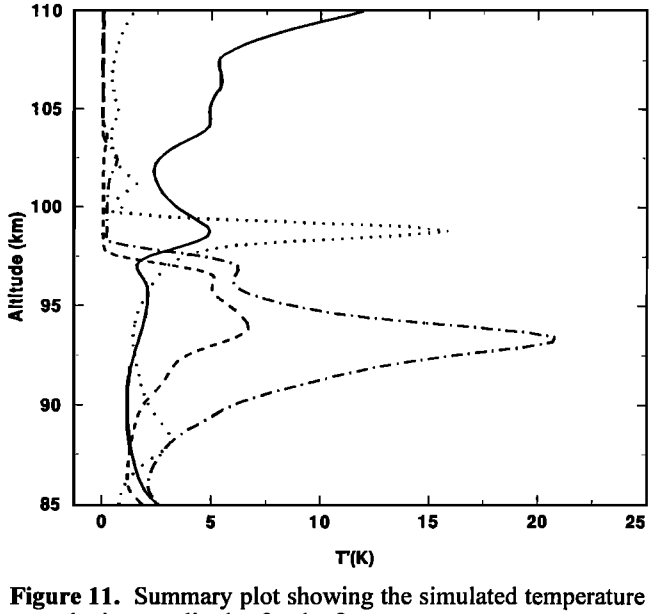

Figure 11. Summary plot showing the simulated temperature perturbation amplitudes for the four waves.

encounter because the region of small wave frequency was very thin compared to the vertical wavelength of the wave. Wave B encountered a critical level near 99 km, which is close to the peak of the O(^1S) emission layer. This wave was not severely attenuated as a result of its critical level encounter primarily because the Richardson number was about 0.25 at the critical level. Waves C and D both encountered two critical levels at similar altitudes (near 97 and 103 km altitude). Both of these waves were severely attenuated at the lowest critical level, which can be attributed to the short vertical wavelength of these waves in the vicinity of the critical level (which varies around the critical region from about 1 to 2 km for both waves) combined with the relatively large (>1) value of the Richardson number at the critical level.

We found that wave A can propagate well into the thermosphere if the mean winds are neglected above about 110 km altitude, but the temperature perturbation amplitude of wave B at 110 km altitude (about 2 K) is significantly less than that of wave A (about 15 K). Waves C and D are unable to propagate into the thermosphere. Unfortunately, there were no observations in the lower thermosphere during ALOHA-93 that would allow us to further constrain our model in order to determine if our simulations were correct. Our results also showed that at lower altitudes (~60 to 80 km) the wave amplitudes were small but nonetheless perhaps detectable. This suggests that future observing campaigns should include instrumentation (such as Rayleigh lidars) to observe this altitude range in order to provide mean winds to further constrain our model and also to attempt to measure gravity waves there.

All four of these waves have similar values of horizontal wavelength, extrinsic period, and extrinsic phase speed (see Table 1). The simulations therefore demonstrate quite convincingly the need for height-resolved, background, mean wind information appropriate for the time and location of the wave observations in order to simulate the observed waves. Furthermore, the fact that the extrinsic wave characteristics are similar for the four waves does not imply similar propagation characteristics for the four waves. Instead, the propagation characteristics of the waves depend sensitively on the mean wind profiles through which the waves propagate. This suggests that the results of (for example) *Swenson et al.* [1995] would be modified quite significantly if the effects of mean winds had been included in their analysis.

We have used a time-independent model to simulate the propagation of gravity waves through mean winds that are in reality time-dependent. This is not an unreasonable assumption because for the wave parameters employed in our study the vertical component of group velocity (several meters per second) calculated from WKB theory implies that the waves propagate through the O(^1S) nightglow emission layer in only a couple of hours or less. This is significantly less than the period of the semidiurnal tide, suggesting that errors associated with the use of static winds may not be bad. However, waves tend to spend more time near critical levels, meaning that time-dependent effects may be important under such conditions.

For each wave that we simulated, we employed the average of the lidar-measured winds for a particular night. We did not investigate the effects of employing slightly different mean wind profiles (for example, employing winds that were 1 standard deviation greater than the means) because the mean profiles changed slowly with time (compared to the gravity wave periods) and because the profiles changed by different amounts at different altitudes. The fact that at any altitude the standard deviation of the winds was significantly smaller than the mean suggests that our use of an average wind profile is well justified.

In this study we did not investigate the effects of changing any of our nominal model parameters, such as diffusion coefficients, the O density profile, or the chemical kinetic parameters. The principal reason for not adjusting these coefficients is that *Hickey et al.* [1997] found that the derived wave amplitudes were determined almost entirely by the mean wind profiles employed in their simulations, with the results being rather insensitive to these other model parameters. Sensitivity studies involving adjustments to these other model parameters will await future study when we attempt to simulate the simultaneous observations of multiple airglow emission fluctuations.

Finally, the Na wind/temperature lidar provided measurements of temperature around the mesopause region. We did not employ these temperatures in our modeling because their effects on the waves will be much less important than the effects of the mean winds. Additionally, the measured temperatures never differed from the MSIS-90 model temperatures by more than about 10%. However, a more complete determination of the sensitivity of our modeling results to the assumed temperature profile in the vicinity of the mesopause will be undertaken at a later time.

6. Conclusions

Our simulations have demonstrated that perturbations in the O(^1S) nightglow emission are sensitive to the mean winds in the O(^1S) emission region. We have also shown how the mean winds influence the propagation of gravity waves from the mesopause region into the lower thermosphere. Particularly important to note is that all of the waves studied had similar extrinsic properties. However, their propagation characteristics were quite dissimilar due to the effects of the different background winds through which the waves propagated. Therefore a complete knowledge of the mean winds is an essential requirement in determining the wave coupling between different atmospheric regions.

Appendix

The O(^1S) chemistry responsible for the green line emission at 557.7 Å is described by the reactions given in Table A1. Here we have assumed, in accordance with *Bates* [1988], that the production of O(^1S) is by a two-step process in which the intermediate state is $O_2(c^1\Sigma_u^-)$. The reaction rates employed here are those given by *Torr et al.* [1985].

The assumption that the mean state is a steady state and use of the above reactions allows us to write for the mean state densities of $O_2(c^1\Sigma_u^-)$ and O(^1S)

$$\bar{n}\left(O_2\left(c^1\Sigma_u^-\right)\right) = \xi k_1 \bar{n}^2(O)\bar{n}(M)/\left\{k_2\bar{n}(O_2) + k_3\bar{n}(O) + A_1\right\} \quad \text{(A1)}$$

$$\bar{n}\left(O\left(^1S\right)\right) = \delta k_3 \bar{n}(O)\bar{n}\left(O_2\left(c^1\Sigma_u^-\right)\right)/\left\{k_6\bar{n}(O_2) + A_3\right\} \quad \text{(A2)}$$

The O profile that we use and the derived OI 557.7 nm emission profile are shown in Figure A1.

Table A1. Chemical Kinetic Parameters Employed in the $O(^1S)$ Nightglow Model

Reaction	Rate of Reaction*
$O + O + M \rightarrow O_2 + M$	$k_1 = 4.7 \times 10^{-33} (300/T)^2$
$O + O + M \rightarrow O_2 (c^1\Sigma_u^-) + M$	$k = \zeta k_1$, $\zeta = 0.03$
$O_2 (c^1\Sigma_u^-) + O_2 \rightarrow O_2 (b^1\Sigma_g^+) + O_2$	$k_2 = 5.0 \times 10^{-13}$
$O_2 (c^1\Sigma_u^-) + O \rightarrow O_2 + O$	$k_3 = 3.0 \times 10^{-11}$ [or 6.0×10^{-12}]
$O_2 (c^1\Sigma_u^-) + O \rightarrow O_2 + O(^1S)$	$k = \delta k_3$, $\delta = 0.2$
$O_2 (c^1\Sigma_u^-) \rightarrow O_2 + h\nu$	$A_1 = 2.0 \times 10^{-2}$ [or 1.0×10^{-3}]
$O(^1S) + O_2 \rightarrow O(^3P) + O_2$	$k_6 = 4.0 \times 10^{-12} \exp(-865/T)$
$O(^1S) \rightarrow O + h\nu$ (5577 Å, 2972 Å)	$A_2 = 1.105$
$O(^1S) \rightarrow O + h\nu$ (5577 Å)	$A_{5577} = 1.06$

* Units are s^{-1}, $cm^{-3}\ s^{-1}$ and $cm^{-6}\ s^{-1}$ for unimolecular, bimolecular, and termolecular reactions, respectively.

Gravity wave perturbations in temperature (T'), velocity divergence ($\underline{\nabla}\cdot\underline{v}'$) and major gas density ($n'(M)$) produce corresponding perturbations in the chemically reactive minor species. We use the method described by *Walterscheid et al.* [1987] to derive the perturbation number densities of O, $O_2(c^1\Sigma_u^-)$, and $O(^1S)$. The fluctuations in O and $O_2(c^1\Sigma_u^-)$ have been described previously by *Hickey et al.* [1993a], while the fluctuations in $O(^1S)$ have been described by *Hickey et al.* [1993b, 1997].

$$\left\{i\omega + 2\bar{k}_1\bar{n}(O)\bar{n}(M)\right\}n'(O) = \bar{n}(O)\left\{(2-f_3)\bar{k}_1\bar{n}(O)\bar{n}(M) - f_1 + f_2/H(O)\right\}T'/\bar{T} \quad \text{(A3)}$$

$$\left\{i\omega + k_2\bar{n}(O_2) + k_3\bar{n}(O) + A_1\right\}n'\left(O_2(c^1)\right) = \left\{2\xi\bar{k}_1\bar{n}(O)\bar{n}(M) - k_3\bar{n}\left(O_2(c^1)\right)\right\}n'(O) + \left\{\begin{array}{l}\xi\bar{k}_1\bar{n}^2(O)\bar{n}(M)(f_3-2) - \bar{n}\left(O_2(c^1)\right) \\ \times\left[k_2\bar{n}(O_2)f_3 - f_1 + f_2/\bar{H}\left(O_2(c^1)\right)\right]\end{array}\right\}\frac{T'}{\bar{T}} \quad \text{(A4)}$$

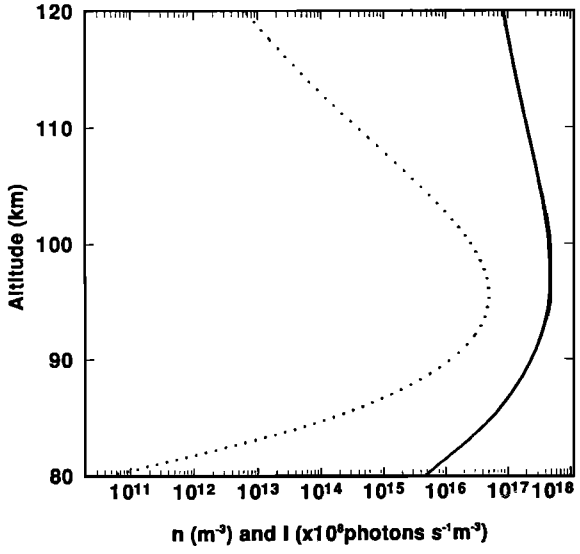

Figure A1. Atomic oxygen density taken from the MSIS-90 model of *Hedin* [1991] for October 7 at 20.8°N (solid line) and derived $O(^1S)$ emission profile (dashed line) employing the chemistry given in the appendix.

$$\left\{i\omega + \bar{k}_6\bar{n}(O_2) + A\right\}n'\left(O(^1S)\right) = \delta k_3\left\{\bar{n}(O)n'\left(O_2(c^1)\right) + \bar{n}\left(O_2(c^1)\right)n'(O)\right\} + \left\{\begin{array}{l}f_2/\bar{H}\left(O(^1S)\right) - f_1 \\ -\bar{k}_6\bar{n}(O_2)\left[\frac{865}{\bar{T}} + f_3\right]\end{array}\right\}\bar{n}\left(O(^1S)\right)\frac{T'}{\bar{T}} \quad \text{(A5)}$$

We have used $\bar{H}(X)$ to denote the scale height of a species X. The complex dynamical factors f_1, f_2, and f_3 relate the temperature perturbation to the velocity divergence, the vertical velocity, and the major gas density perturbation, respectively, such that

$$\underline{\nabla}\cdot\underline{v}' = f_1 T'/\bar{T} \quad \text{(A6)}$$

$$w' = f_2 T'/\bar{T} \quad \text{(A7)}$$

$$n'(M)/\bar{n}(M) = f_3 T'/\bar{T} \quad \text{(A8)}$$

The emission intensity of the $O(^1S)$ is proportional to $A_{5577}n(O(^1S))$ and so it follows that the fractional emission fluctuation at a specific altitude is equal to $n'(O(^1S))/\bar{n}(O(^1S))$. The observed fractional emission fluctuation is obtained by integrating both the numerator and denominator over the vertical extent of the emission, giving

$$\langle\delta I\rangle/\langle\bar{I}\rangle = \int_{-\infty}^{\infty} n'\left(O(^1S)\right)dz \Big/ \int_{-\infty}^{\infty} \bar{n}\left(O(^1S)\right)dz \quad \text{(A9)}$$

In practice, we only needed to integrate between 75 and 130 km altitude to accurately define $\langle\delta I\rangle/\langle\bar{I}\rangle$.

Acknowledgments. The support by the National Science Foundation of the ALOHA-93 campaign is greatly appreciated. MPH was supported by NSF grant ATM-9402434 and NASA grant NAGW-3979, and CSG was supported by NSF grant ATM-9403036. We are grateful to Thermo Trex corporation, for arranging our use of the AMOS and DOE facilities on Haleakala for the joint measurements. The Utah State University measurements were supported by NSF grant ATM-9302844. Support for the image analysis was provided by NSF grant ATM-9525815 and by the Geophysics Directorate, Air Force Phillips Laboratory, contract F19628-93-C-0165 as part of the SOAR program. We wish to thank Richard Walterscheid and Gerald Schubert for fruitful discussions during the development of the full-wave model, and also appreciate discussions with Xin Tao, Miguel Larsen and Tom Slanger. The reviewers comments are also gratefully acknowledged.

References

Andreassen, Ø., C. E. Wasberg, D. C. Fritts, and J. R. Isler, Gravity wave breaking in two and three dimensions, 1, Model description and comparison of two-dimensional evolutions, *J. Geophys. Res., 99*, 8095, 1994.

Bates, D. R., Excitation of 557.7 nm OI line in nightglow, *Planet. Space Sci., 36*, 883, 1988.

Breeding, R. J., A non-linear investigation of critical levels for internal atmospheric gravity waves, *J. Fluid Mech., 50*, 545, 1971.

Bretherton, F. P., and C. J. R. Garrett, Wave trains in inhomogeneous moving media, *Proc. R. Soc. London, Ser. A, 302*, 529, 1968.

Bruce, C. H., D. W. Peaceman, H. H. Rachford Jr., and J. P. Rice, Calculations of unsteady-state gas flow through porous media, *Petrol. Trans. AIME, 198*, 79-92, 1953.

Cowling, D. H., H. D. Webb, and K. C. Yeh., Group rays of internal gravity waves in a wind-stratified atmosphere, *J. Geophys. Res., 76*, 213, 1971.

Dao, P. D., R. Farley, X. Tao, and C. S. Gardner, Lidar observations of the temperature profile between 25 and 103 km: Evidence of strong tidal perturbation, *Geophys. Res. Lett., 22*, 2825, 1995.

Fritts, D. C., Gravity wave saturation in the middle atmosphere: A review of theory and observations, *Rev. Geophys., 22*, 275, 1984.

Garcia, F. J., M. J. Taylor, and M. C. Kelley, Two-dimensional spectral analysis of airglow image data, *Appl. Opt., 36*, 7374-7385, 1997.

Gardner, C. S., X. Tao, and G. C. Papen, Simultaneous lidar observations of vertical wind, temperature, and density profiles in the upper mesosphere: Evidence for nonseperability of atmospheric perturbation spectra, *Geophys. Res. Lett., 22*, 2877, 1995.

Hedin, A. E., Extension of the MSIS thermosphere model into the middle and lower atmosphere, *J. Geophys. Res., 96*, 1159, 1991.

Hickey, M. P., and K. D. Cole, A quartic dispersion equation for internal gravity waves in the thermosphere, *J. Atmos. Terr. Phys., 49*, 889, 1987.

Hickey, M. P., G. Schubert, and R. L. Walterscheid, Gravity wave-driven fluctuations in the O_2 Atmospheric (0-1) nightglow from an extended, dissipative emission region, *J. Geophys. Res., 98*, 13,717-13,730, 1993a.

Hickey, M. P., R. L. Walterscheid, and G. Schubert, A model of wave-driven fluctuations in the O(^1S) nightglow, *E Trans AGU, 74*(16), Spring Meeting Suppl., 218, 1993b.

Hickey, M. P., R. L. Walterscheid and G. Schubert, A numerical model of gravity wave propagation in an inhomogeneous atmosphere, *E Trans. AGU, 75*(44), Fall Meeting Suppl., 508, 1994.

Hickey, M. P., R. L. Walterscheid and G. Schubert, The propagation and dissipation of gravity waves in the terrestrial atmosphere: Full-wave versus WKB models, *E Trans. AGU, 76*(46), Fall Meeting Suppl., F436, 1995.

Hickey, M. P., R. L. Walterscheid, M. J. Taylor, W. Ward, G. Schubert, Q. Zhou, F. Garcia, M. C. Kelley, and G. G. Shepherd, Numerical simulations of gravity waves imaged over Arecibo during the 10-day January 1993 campaign, *J. Geophys. Res., 102*, 11,475, 1997.

Lindzen, R. S., Internal gravity waves in atmospheres with realistic dissipation and temperature, I, Mathematical development and propagation of waves into the thermosphere, *Geophys. Fluid Dyn., 1*, 303-355, 1970.

Lindzen, R. S., Turbulence and stress owing to gravity wave and tidal breakdown, *J. Geophys. Res., 86*, 9707, 1981.

Orlanski, I., and K. Bryan, Formation of the thermocline step structure by large-amplitude internal gravity waves, *J. Geophys. Res., 74*, 6975, 1969.

Rees, M. H., *Physics and Chemistry of the Upper Atmosphere*, Cambridge Univ. Press, New York, 1989.

Schubert, G., and R. L. Walterscheid, Wave-driven fluctuations in OH nightglow from an extended source region, *J. Geophys. Res., 93*, 9903-9915, 1988.

Schubert, G., R. L. Walterscheid, and M. P. Hickey, Gravity wave-driven fluctuations in OH nightglow from an extended, dissipative emission region, *J. Geophys. Res., 96*, 13,869-13,880, 1991.

Strobel, D. F., Constraints on gravity wave induced diffusion in the middle atmosphere, *Pure Appl. Geophs., 130*, 533, 1989.

Swenson, G. R., C. S. Gardner, and M. J. Taylor, Maximum altitude penetration of atmospheric gravity waves observed during ALOHA-93, *Geophys. Res. Lett., 22*, 2857, 1995.

Tao, X., and C. S. Gardner, Heat flux observations in the mesopause region above Haleakala, *Geophys. Res. Lett., 22*, 2829, 1995.

Taylor, M. J., and F. J. Garcia, A two-dimensional spectral analysis of short period gravity waves imaged in the OI(557.7 nm) and near-infrared OH nightglow emissions over Arecibo, Puerto Rico, *Geophys. Res. Lett., 22*, 2473, 1995.

Taylor, M. J., E. H. Ryan, T. F. Tuan, and R. Edwards, Evidence of preferential directions for gravity wave propagation due to wind filtering in the middle atmosphere, *J. Geophys. Res., 98*, 6047, 1993.

Taylor, M. J., W. R. Pendleton Jr., S. Clark, H. Takahashi, D. Gobii, and R. A. Goldberg, Image measurements of short period gravity waves at equatorial latitudes, *J. Geophys. Res., 102*, 26,283-26,299, 1997.

Torr, M. R., D. G. Torr, and R. R. Laher, The O_2 atmospheric 0-0 band and related emissions at night from Spacelab 1, *J. Geophys Res., 90*, 8525, 1985.

Walterscheid, R. L., and G. Schubert, Nonlinear evolution of an upward propagating gravity wave: Overturning, convection, transience and turbulence, *J. Atmos. Sci., 47*, 101-125, 1990.

Walterscheid, R. L., G. Schubert, and J. M. Straus, A dynamical-chemical model of wave-driven fluctuations in the OH nightglow, *J. Geophys. Res., 92*, 1241-1254, 1987.

Ward, W. E., D. Y. Wang, B. H. Solheim, and G. G. Shepherd, Observations of the two-day wave in WINDII data during January 1993, *Geophys. Res. Lett., 23*, 2923-2926, 1996.

C. S. Gardner, Department of Electrical and Computer Enginerring, University of Illinois, Urbana, IL 61801. (E-mail: cgardner@uiuc.edu)

C. R. Gibbons and M. P. Hickey, Center for Space Plasma, Aeronomy and Astrophysics Research, University of Alabama, Huntsville, AL 35899. (E-mail: hickeym@cspar.uah.edu)

M. J. Taylor, Space Dynamics Laboratory, Utah State University, Logan, UT 84322. (E-mail: mtaylor@cc.usu.edu)

(Received January 22, 1997; revised June 23, 1997;
accepted November 19, 1997.)